CENTRE FOR **STOCHASTIC GEOMETRY**
AND ADVANCED **BIOIMAGING**

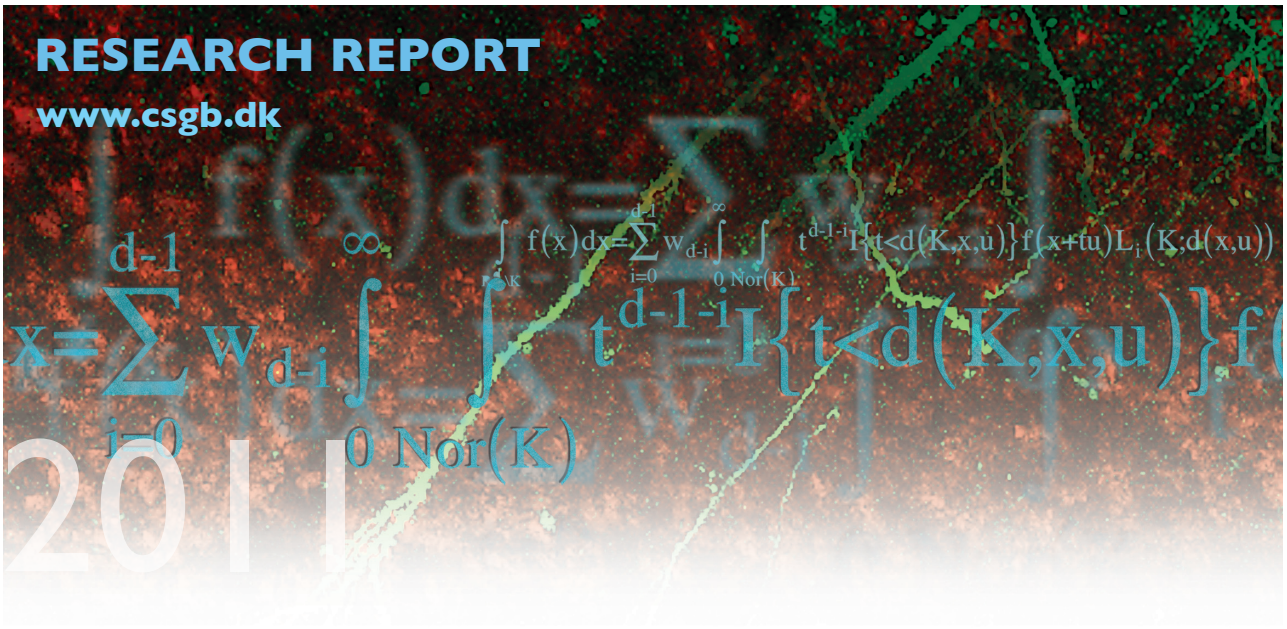

Kristjana Yr Jonsdottir, Anders Rønn-Nielsen, Kim Mouridsen
and Eva B. Vedel Jensen

Lévy Based Modelling in Brain Imaging

No. 02, April 2011

Lévy Based Modelling in Brain Imaging

Kristjana Yr Jonsdottir[1,2], Anders Rønn-Nielsen[3], Kim Mouridsen[1] and Eva B. Vedel Jensen[2,4]

[1]Center of Functionally Integrative Neuroscience, Aarhus University
[2]Department of Mathematical Sciences, Aarhus University
[3]Department of Mathematical Sciences, University of Copenhagen
[4]Centre for Stochastic Geometry and Advanced Bioimaging, Aarhus University

Abstract

Traditional methods of analysis in brain imaging based on Gaussian random field theory may leave small, but significant changes in the signal level undetected, because the assumption of Gaussianity is not fulfilled. In group comparisons, the number of subjects in each group is usually small so the alternative strategy of using a non-parametric test may not be appropriate either because of low power. We propose to use a flexible, yet tractable model for a random field, based on kernel smoothing of a so-called Lévy basis. The resulting field may be Gaussian but there are many other possibilities, e.g. random fields based on Gamma, inverse Gaussian and normal inverse Gaussian (NIG) Lévy bases. We show that it is easy to estimate the parameters of the model and accordingly to assess by simulation the quantiles of a test statistic. A finding of independent interest is the explicit form of the kernel function that induces a covariance function belonging to the Matérn family.

Keywords: Covariance, cumulant, Gaussian random field, Matérn covariance function, non-Gaussian random field, normal inverse Gaussian Lévy basis

1 Introduction

Neuroimaging studies typically aim to detect localized changes in brain structure, physiology, or neuronal activity attributable to disease and/or therapeutic intervention. Positron emission tomography (PET) is the current gold standard for imaging key physiological markers such as cerebral blood flow and blood volume, but such measures can also be obtained without the use of radioactive tracers using MRI. Additionally MRI can produce high resolution images of brain anatomy. Further, MRI is used intensively in the study of human brain function (fMRI) where serial images are acquired while subjects perform specific mental tasks.

To enable detection of regional changes, the measure of interest is recorded in each volume element (voxel) of the brain. In group comparisons, such a field of

Corresponding author: Kristjana Yr Jonsdottir, kyj@imf.au.dk

measurements is obtained for each subject belonging to a disease/treatment group and a control group. Typically, a $t-$test of the hypothesis of no difference between the two groups is performed at each voxel, resulting in a field of thousands of correlated $t-$statistics.

To control the false positive rate, various methods to evaluate the field of test statistics have been proposed. A very useful review of these methods can be found in Nichols and Hayasaka (2003). Apart from the Bonferroni procedure that usually disregards the dependence of the test statistics, methods based on random field theory (Worsley 1994, Worsley et al. 1992, Worsley et al. 1996) are very popular. Under the assumption that the random field is Gaussian or Gaussian derived, the $P-$value of the maximum of the field can be approximated by the expected Euler characteristic of the excursion set. An alternative to the maximum is to consider under a Gaussian assumption the size of the largest connected component of the excursion set (Cao 1999). It is, however, wellknown that the Gaussian assumption of the random field may be too restrictive, cf. Salmond et al. (2002), Viviani et al. (2007) and references therein. Furthermore, it has been shown that the geometry of excursion sets is considerably more complicated for non-Gaussian random fields than for Gaussian random fields (Adler et al. 2010a,b).

Unfortunately, there are at the moment no methods of evaluating the robustness of this analysis against the departures from Gaussianity seen in a concrete data set. In group comparisons, an alternative is to use a permutation test (Nichols and Holmes 2001) but this test may have low power in the cases where the number of subjects in each group is small, as is typical. This is exactly the situation where departures from Gaussianity may affect most severely the null distribution of the field of test statistics.

The present paper takes up this problem. We propose a flexible, yet tractable model for a random field, based on kernel smoothing of a Lévy basis, an independently scattered, infinitely divisible random measure. (The short terminology of a Lévy basis has been introduced in Barndorff-Nielsen and Schmiegel (2004), see also Wolpert (2001)). This type of model has earlier been used with success in modelling of turbulence (Barndorff-Nielsen and Schmiegel 2004), Cox point processes (Hellmund et al. 2008) and growth (Jónsdóttir et al. 2008). We derive the kernel function that induces the flexible Matérn covariance function (Guttorp and Gneiting 2006). Earlier, specific covariance functions such as the exponential and Gaussian covariance functions have been considered in Bowman (2007) and Spence et al. (2007). The Lévy basis may be Gaussian but there are many other possibilities, e.g. Gamma, inverse Gaussian and normal inverse Gaussian to name a few. We show that it is easy to estimate the parameters of the model and accordingly to assess by simulation the quantiles of the distribution of the maximum of the field of test statistics.

Furthermore, we expect that the proposed extended random field model will have independent interest in functional neuroimaging. Gaussian random fields only focus on the mean, variance and covariance. Interesting changes due to disease or therapy that imply that the distribution of the measurement has more heavy tails or is more skewed can only be modelled if one goes beyond Gaussianity.

The present paper is organized as follows. In Section 2, we give a short introduction to Gaussian random fields and the notation used for covariances and cumulants,

while Section 3 gives a number of examples of kernel functions and their induced covariance functions. In particular, the kernel function, inducing a covariance function belonging to the Matérn family, is given in Section 3. In Section 4, we give an example of brain imaging data that cannot be described satisfactory by a Gaussian random field. This motivates us to consider Lévy based random fields and their statistical inference in Sections 5 and 6. The data set is reanalyzed, using a model based on the normal inverse Gaussian distribution in Section 7 and consequences for brain imaging are discussed in Section 8. Our findings are put into further perspective in Section 9. The derivation of the kernel function that induces the Matérn covariance function is deferred to the Appendix.

2 Gaussian random fields, covariances and cumulants

Let x_v be the observation at the site (pixel or voxel) with coordinate $v \in \mathcal{V}$, where $\mathcal{V}$ is a bounded subset of $\mathbb{R}^d$, $d = 2$ or 3.

In case $\mathcal{V} \subseteq \mathbb{Z}^d$, a simple example of a Gaussian random field is given by the following equation

$$X_v = \sum_{u \in \mathbb{Z}^d} k(v, u) Z_u, \tag{2.1}$$

where k is a kernel function and the Z_us are independent and identically distributed Gaussian random variables. This type of model is very similar to moving average models for time series (Gaetan and Guyon 2010, Section 1.7.1, Wolpert 2001).

Let Z be a random variable with the common distribution of the Z_us. Under the model (2.1), the covariances take the form

$$\operatorname{Cov}(X_{v_1}, X_{v_2}) = \operatorname{Var}(Z) \sum_{u \in \mathbb{Z}^d} k(v_1, u) k(v_2, u), \tag{2.2}$$

while the cumulants of the random variables X_v can be expressed as

$$\kappa_n(X_v) = \kappa_n(Z) \sum_{u \in \mathbb{Z}^d} k(v, u)^n, \quad n = 1, 2, \ldots, \tag{2.3}$$

since the X_vs are linear combinations of independent random variables.

The model (2.1) may be formulated continuously as

$$X_v = \int_{\mathbb{R}^d} k(v, u) Z(\mathrm{d}u), \tag{2.4}$$

where Z is an independently scattered, stationary Gaussian random measure (Gaetan and Guyon 2010, Section 1.5.1). It turns out that under mild regularity conditions any Gaussian random field can be described in this fashion, cf. e.g. Hellmund et al. (2008, Proposition 6).

Suppose that

$$Z(\mathrm{d}u) \sim N(\mu \, \mathrm{d}u, \tau^2 \, \mathrm{d}u),$$

and let $Z' \sim N(\mu, \tau^2)$. Then, under the continuous formulation (2.4), (2.2) takes the form

$$\operatorname{Cov}(X_{v_1}, X_{v_2}) = \operatorname{Var}(Z') \int_{\mathbb{R}^d} k(v_1, u) k(v_2, u) \, \mathrm{d}u. \tag{2.5}$$

Furthermore, (2.3) becomes

$$\kappa_n(X_v) = \kappa_n(Z') \int_{\mathbb{R}^d} k(v, u)^n \, \mathrm{d}u, \quad n = 1, 2, \ldots. \tag{2.6}$$

Covariances and cumulants of X_v can thus directly be expressed in terms of the cumulants of Z', if the relevant integrals of the kernel function can be calculated explicitly.

In the remaining part of the paper, we will assume that $k(u, v) = k(u - v)$, say, and that

$$\int_{\mathbb{R}^d} k(u) \, \mathrm{d}u = 1.$$

If we let

$$K(v) = \int_{\mathbb{R}^d} k(u) k(v + u) \, \mathrm{d}u,$$

then

$$\operatorname{Cov}(X_{v_1}, X_{v_2}) = \operatorname{Var}(Z') K(v_1 - v_2).$$

If $K(v) = K(\|v\|)$, say, the covariance

$$\operatorname{Cov}(X_{v_1}, X_{v_2}) = C(\|v_1 - v_2\|) = \operatorname{Var}(Z') K(\|v_1 - v_2\|)$$

depends only on the distance between sites. The correlation function takes the form

$$\rho(h) = K(h)/K(0), \; h \geq 0.$$

The variogram γ, defined as $\mathbb{E}(X_{v_1} - X_{v_2})^2$, depends in this case also only on the distance between sites and can be expressed as

$$\gamma(h) = 2 \operatorname{Var}(Z')(K(0) - K(h)).$$

A normalized version of the variogram is

$$\bar{\gamma}(h) = \gamma(h) / \operatorname{Var}(X_v) = 2(1 - \rho(h)).$$

3 Covariance models

In this section, we give examples of kernel functions k and induced covariance structures determined by K. For further details, see Cressie (1993) and Gaetan and Guyon (2010, Section 1.5.1). We also give the explicit form of $\int_{\mathbb{R}^d} k(v, u)^n \, \mathrm{d}u$ for the different kernels when possible. The kernel function that induces the general Matérn covariance model, see Example 3 below, is to the best of our knowledge not available in the literature.

Example 1 (Spherical covariance)**.** Suppose that

$$k(u,v) = \mathbf{1}[\|u-v\| \le R]/|B(0,R)|.$$

Then, if $\omega \in S^{d-1}$ is a unit vector in $\mathbb{R}^d$,

$$K(h) = \frac{|B(0,R) \cap B(h\omega,R)|}{|B(0,R)|^2}$$

and

$$\int_{\mathbb{R}^d} k(v,u)^n \, \mathrm{d}u = |B(0,R)|^{-n+1}.$$

For $d = 3$, we get

$$K(h) = \frac{1}{|B(0,R)|}\left(1 + \frac{h}{4R}\right)\left(1 - \frac{h}{2R}\right)^2 \mathbf{1}[h \le 2R].$$

Example 2 (Gaussian covariance)**.** Suppose that

$$k(u,v) = \frac{1}{(2\pi\sigma^2)^{d/2}} \exp\left(-\frac{1}{2\sigma^2}\|u-v\|^2\right).$$

Then,

$$K(h) = \frac{1}{(4\pi\sigma^2)^{d/2}} \exp\left(-\frac{1}{4\sigma^2}h^2\right)$$

and

$$\int_{\mathbb{R}^3} k(v,u)^n \, \mathrm{d}u = n^{-d/2}(2\pi\sigma^2)^{-d(n-1)/2}.$$

Example 3 (Matérn covariance)**.** In the Appendix, we derive the kernel function that induces a covariance function belonging to the Matérn family, see Guttorp and Gneiting (2006) and references therein. It is shown that if

$$k(u,v) = \frac{\lambda^d}{\pi^{d/2}2^{\nu/2-1+3d/4}\Gamma\left(\frac{\nu+d/2}{2}\right)}\|\lambda(u-v)\|^{\nu/2-d/4}K_{\nu/2-d/4}(\lambda\|u-v\|), \qquad (3.1)$$

then

$$K(h) = \frac{\lambda^d}{\pi^{d/2}2^{d+\nu-1}\Gamma(\nu+d/2)}(\lambda h)^\nu K_\nu(\lambda h). \qquad (3.2)$$

Here, K_ν is the modified Bessel function of the second kind, and λ and ν are positive parameters.

As shown in the supplement file, the flexible Matérn covariance family includes a number of well-known covariance functions. Let us concentrate on the 3D case, i.e. $d = 3$. For $d = 3$ and $\nu = \frac{1}{2}$, (3.1) becomes

$$k(u,v) = \frac{\lambda^2}{4\pi\|u-v\|}\exp\left(-\lambda\|u-v\|\right),$$

and (3.2) is the exponential covariance function

$$K(h) = \frac{\lambda^3}{8\pi} \exp\left(-\lambda h\right).$$

For $d = 3$ and $\nu = \frac{5}{2}$, the kernel function (3.1) is of the form

$$k(u, v) = \frac{\lambda^3}{8\pi} \exp\left(-\lambda \|u - v\|\right),$$

and (3.2) is the 3rd order autoregressive covariance function

$$K(h) = \frac{\lambda^3}{64\pi} \exp\left(-\lambda h\right) \left(\frac{\lambda^2}{3} h^2 + \lambda h + 1\right).$$

In order to evaluate the cumulant relation (2.6), we will also need to evaluate $\int_{\mathbb{R}^d} k(v, u)^n \, \mathrm{d}u$. For $n = 2$, we get, see the Appendix,

$$\int_{\mathbb{R}^d} k(v, u)^2 \, \mathrm{d}u = \frac{\lambda^d \Gamma(\nu)}{2^d \pi^{d/2} \Gamma(\nu + d/2)}. \tag{3.3}$$

For $n > 2$, it can be shown that

$$\int_{\mathbb{R}^d} k(v, u)^n \, \mathrm{d}u < \infty \quad \text{for } \nu > \nu(d, n),$$

where the limit $\nu(d, n)$ depends on n and d: $\nu(2, 3) = \frac{1}{3}$, $\nu(2, 4) = \frac{1}{2}$, $\nu(3, 3) = \frac{1}{2}$ and $\nu(3, 4) = \frac{3}{4}$. In particular, for the exponential covariance model in $\mathbb{R}^3$ ($d = 3, \nu = \frac{1}{2}$), we get

$$\int_{\mathbb{R}^3} k(v, u)^n \, \mathrm{d}u = \infty, \quad n > 2,$$

Analytic forms of the integrals $\int_{\mathbb{R}^d} k(v, u)^n \, \mathrm{d}u$ can be derived for some parameter values, in other cases the integrals have to be evaluated numerically. For the 3rd order autoregressive model in $\mathbb{R}^3$ ($d = 3, \nu = \frac{5}{2}$), we have

$$\int_{\mathbb{R}^3} k(v, u)^n \, \mathrm{d}u = \frac{1}{n^3} \left(\frac{\lambda^3}{8\pi}\right)^{n-1}, \quad n \geq 2. \tag{3.4}$$

Note that the last equation also holds for $n = 2$. Further details are provided in the Appendix.

4 Data example

We obtained dynamic susceptibility contrast magnetic resonance imaging (MRI) scans from four healthy subjects (1.5 Tesla, gradient echo, TR/TE = 1500 ms/30 ms). From these scans, maps of vascular mean transit time (MTT), were calculated using singular value decomposition (Wu et al. 2003; Østergaard et al. 1996). The MTT measurements are recognized as a valuable indicator of the cerebral blood circulation (Helenius et al. 2003; Ibaraki et al. 2007; Ito et al. 2003). While MTT is at a stable

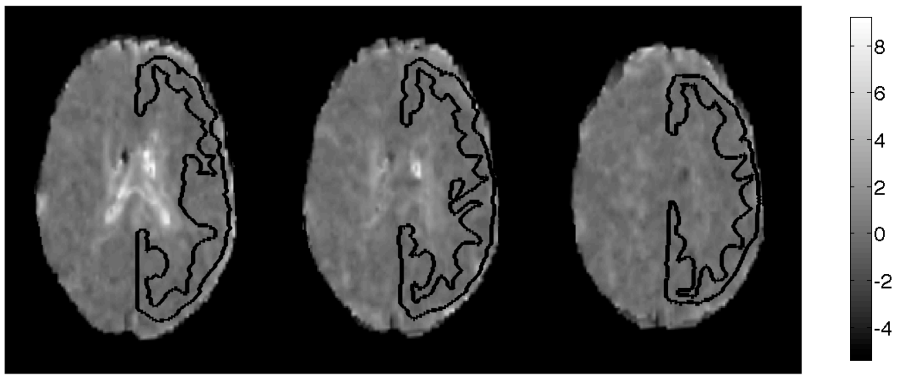

Figure 1: MTT images. The trace of the cortical region on the three slices under study is delineated by the black curve.

level throughout the cortical region in healthy subjects, changes may appear in specific cortical regions in patients with certain diseases such as cerebrovascular diseases, Alzheimer's disease and multiple sclerosis (Adhya et al. 2006; Luckhaus et al. 2008; Lythgoe et al. 2000).

The data to be analyzed for each of the four healthy subjects are MTT measurements from three slices through the right side of the cortical region. The voxels have dimension 1 mm × 1 mm × 1 mm, the distance between neighbour slices is 10 mm. Figure 1 shows the boundary of the cortical region on the three slices under study. Note the extensive boundary of the region under study which is typical in brain imaging. The total number of voxels in the studied region was 8882. All analysis and simulations presented were performed in MATLAB 7.9.0 (R2009b).

In Figure 2, we show for each of the four subjects the estimated variogram normalized with the empirical variance, see Section 6 for further details. We fitted by least squares a Matérn covariance model to the normalized variograms as this model was superior to both the spherical model and the Gaussian covariance model. The corresponding parametric fits of the normalized variogram are also shown in Figure 2.

The remaining unknown parameters of the Gaussian random field model (2.4) are μ (the mean value of Z') and τ^2 (the variance of Z'). These parameters can be estimated from $\mathbb{E}(X_v)$ and $\mathrm{Var}(X_v)$. For a 3D image ($d = 3$), we get, using (2.6) and (3.3),

$$\begin{aligned} \mathbb{E}(X_v) &= \mu \\ \mathrm{Var}(X_v) &= \tau^2 \frac{\lambda^3 \Gamma(\nu)}{8\pi^{3/2}\Gamma(\nu + 3/2)}. \end{aligned} \tag{4.1}$$

Substituting $\mathbb{E}(X_v)$ and $\mathrm{Var}(X_v)$ by their empirical analogues gives us an estimate of the parameters μ and τ^2. Since we subtracted the average $\bar{x}.$ from the measurement x_v in each voxel, $\hat{\mu} = 0$ for all the four subjects. The estimates of the standard deviation τ and the parameters ν and λ of the kernel function of the Matérn model are shown in Table 1 for each of the four subjects.

A closer look at the observed distribution of X_v shows systematic departures from the Gaussian distribution, especially for subject 4, see Figure 3. The observed

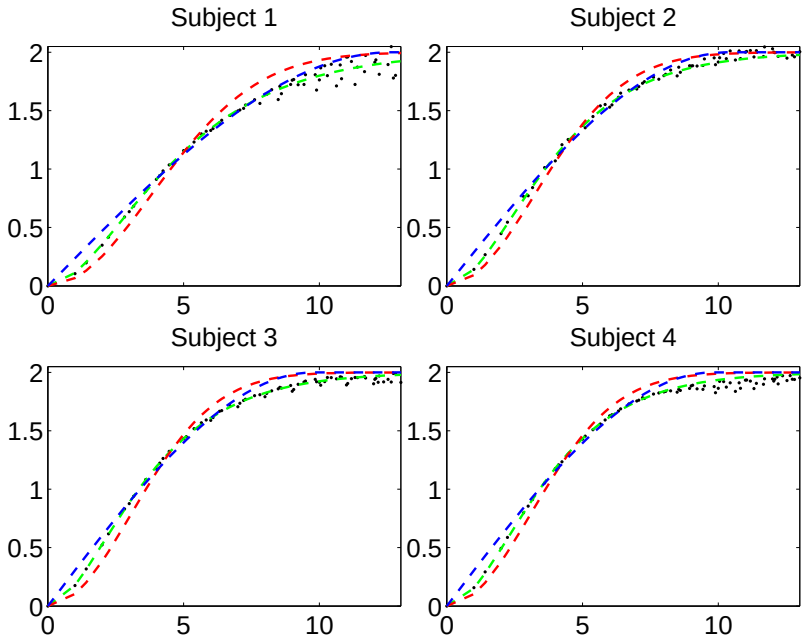

Figure 2: The estimated normalized variogram of the four subjects (·), together with a fitted Matérn variogram model (green stippled line). The fitted variogram under the Gaussian covariance model (red stippled line) and the spherical covariance model (blue stippled line) are also shown.

Table 1: The estimates of the parameters of a Gaussian random field model with a Matérn covariance structure.

Subject	$\hat{\tau}$	$\hat{\nu}$	$\hat{\lambda}$
1	21.7136	1.5700	0.3971
2	11.0862	1.9345	0.5477
3	14.9562	1.5660	0.5162
4	13.4618	2.0054	0.5938

distributions are markedly right skewed. There is therefore a need to go beyond the Gaussian random field model.

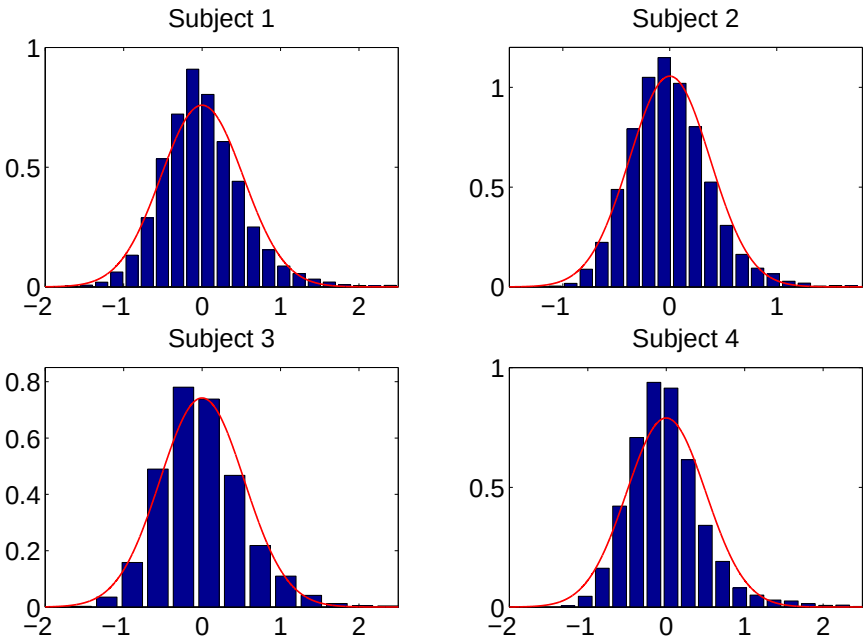

Figure 3: Histograms for the data in the selected region for four healthy subjects together with the fitted Gaussian density. The average $\bar{x}.$ has been subtracted from the measurement in each voxel. Note that the observed distributions are markedly right skewed.

5 Lévy based random fields

In this section, we consider more general random fields defined by the equation

$$X_v = \sum_{u \in \mathbb{Z}^d} k(v,u) Z_u, \tag{5.1}$$

where the Z_us still are independent and identically distributed *but* not necessarily Gaussian. The common distribution of the Z_us is assumed to be infinitely divisible. Possible choices of the distribution of the Z_us are the Gaussian distribution, the Gamma distribution, the inverse Gaussian distribution and the normal inverse Gaussian distribution. The moment relations (2.2)–(2.3) still hold with Z being a random variable with the common distribution of the Z_us.

There also exists a continuous formulation of (5.1)

$$X_v = \int_{\mathbb{R}^d} k(v,u) Z(\mathrm{d}u), \tag{5.2}$$

where Z is an independently scattered infinitely divisible random measure. Such a measure is called a Lévy basis, cf. Hellmund et al. (2008) and references therein. Associated with Z is a random variable Z', called the spot variable. In the Gaussian case, we have

$$Z(\mathrm{d}u) \sim N(\mu \, \mathrm{d}u, \tau^2 \, \mathrm{d}u), \quad Z' \sim N(\mu, \tau^2)$$

such that

$$\kappa_1(Z') = \mu, \quad \kappa_2(Z') = \tau^2, \quad \kappa_3(Z') = \kappa_4(Z') = 0.$$

Corresponding characteristics are given for the Gamma, the inverse Gaussian and the normal inverse Gaussian bases in Table 2.

Table 2: The spot variable and its cumulants for various Lévy bases.

Basis $Z(\mathrm{d}u)$	Gamma $\Gamma(\alpha\,\mathrm{d}u, \lambda)$	Inverse Gaussian $\mathrm{IG}(\delta\,\mathrm{d}u, \gamma)$	Normal Inverse Gaussian $\mathrm{NIG}(\alpha, \beta, \mu\,\mathrm{d}u, \delta\,\mathrm{d}u)$
Z'	$\Gamma(\alpha, \lambda)$	$\mathrm{IG}(\delta, \gamma)$	$\mathrm{NIG}(\alpha, \beta, \mu, \delta)$
$\kappa_1(Z')$	α/λ	δ/γ	$\mu + \delta\beta/(\alpha^2 - \beta^2)^{1/2}$
$\kappa_2(Z')$	α/λ^2	δ/γ^3	$\delta\alpha^2/(\alpha^2 - \beta^2)^{3/2}$
$\kappa_3(Z')$	$2\alpha/\lambda^3$	$3\delta/\gamma^5$	$3\delta\beta\alpha^2/(\alpha^2 - \beta^2)^{5/2}$
$\kappa_4(Z')$	$6\alpha/\lambda^4$	$15\delta/\gamma^7$	$3\delta(\alpha^2 + 4\beta^2)\alpha^2/(\alpha^2 - \beta^2)^{7/2}$

It is important that the moment relations (2.5) and (2.6) still hold for the model (5.2) so that model parameters may be expressed in terms of the moments of X_v also in the non-Gaussian case.

Note that if the Lévy basis Z is stationary and $k(u, v) = k(u - v)$, then $\{X_v\}_{v \in \mathcal{V}}$ is the restriction to $\mathcal{V}$ of a stationary process. In particular, the distribution of X_v is the same at the boundary as in the interior of $\mathcal{V}$. This may be an important feature when $\mathcal{V}$ has an extensive boundary as is typical in brain imaging.

For any of the bases listed in Table 2 and any bounded Borel subset A of $\mathbb{R}^d$, the distribution of $Z(A)$ is as indicated by the name of the basis. For instance, for a normal inverse Gaussian basis,

$$Z(A) \sim \mathrm{NIG}\big(\alpha, \beta, \mu\lambda_d(A), \delta\lambda_d(A)\big),$$

where λ_d is the notation used for Lebesgue measure in $\mathbb{R}^d$, cf. Barndorff-Nielsen (1998). It follows that if the kernel function in (5.2) is proportional to an indicator function as for the spherical covariance model, see Section 3, then the marginal distribution of X_v will be of the type indicated by the name of the Lévy basis. Otherwise, the marginal distribution of X_v will not be as simple but still we will adopt the name of the Lévy basis. For instance, if Z is a normal inverse Gaussian Lévy basis, the random field defined by (5.2) will be called a normal inverse Gaussian random field irrespectively of the choice of kernel function.

Note that if Z is a normal inverse Gaussian Lévy basis, then conditionally on a Inverse Gaussian Lévy basis L, $L(A) \sim \mathrm{IG}(\delta\lambda_d(A), \sqrt{\alpha^2 - \beta^2})$, we have that X_v is a Gaussian random field

$$X_v \mid L \sim \int_{\mathbb{R}^d} k(u, v) Z_0(\mathrm{d}u),$$

where Z_0 is a Gaussian Lévy basis with $Z_0(A) \sim N(\mu\lambda_d(A) + \beta L(A), L(A))$. In particular, $\{X_v : v \in \mathcal{V}\}$ can be seen as a Gaussian random field with a stochastic

mean field $\{\mu + \beta M_v : v \in \mathcal{V}\}$ and a stochastic variance field $\{S_v : v \in \mathcal{V}\}$, where $\{M_v : v \in \mathcal{V}\}$ and $\{S_v : v \in \mathcal{V}\}$ are correlated inverse Gaussian random fields

$$M_v = \int k(u, v) L(\mathrm{d}u), \quad S_v = \int k(u, v)^2 L(\mathrm{d}u).$$

For more details, cf. Barndorff-Nielsen (2010) and Barndorff-Nielsen and Pedersen (2010).

6 Inference

The parameters of the kernel function can be estimated from the variogram of the observed image. If $\{x_v : v \in \mathcal{V}\}$ are the available data, then, cf. Cressie (1993),

$$\frac{1}{|N(d)|} \sum_{(i,j) \in N(d)} (x_{v_i} - x_{v_j})^2 / \hat{\kappa}_2(x_v) \tag{6.1}$$

is an estimate of the normalized variogram

$$\bar{\gamma}(d) = 2(1 - \rho(d)) = 2(1 - K(d)/K(0)).$$

Here, $N(d)$ is the set of pairs of indices of sites with mutual distance d, $|N(d)|$ is the number of such pairs and $\hat{\kappa}_2(X_v)$ is the empirical variance in the observed image, see (6.2) below. Since the normalized variogram is uniquely determined by the parameters of the kernel function we can determine estimates of these parameters from the estimate (6.1) of the normalized variogram.

The basis for obtaining the estimates of the parameters of the Lévy basis is the cumulant relations (2.6). The actual values of the integrals $\int_{\mathbb{R}^3} k(v, u)^n \, \mathrm{d}u$ can be found in Section 3 for the various covariance models. In order to use the cumulant relations we need estimates of the cumulants of X_v. This can either be done non-parametrically by using the following equations, cf. Kendall and Stuart (1976, p. 299),

$$\begin{aligned}
\hat{\kappa}_1(X_v) &= \frac{1}{n} S_1 \\
\hat{\kappa}_2(X_v) &= \frac{1}{n(n-1)} (n S_2 - S_1^2) \\
\hat{\kappa}_3(X_v) &= \frac{1}{n(n-1)(n-2)} (n^2 S_3 - 3n S_2 S_1 + 2 S_1^3) \\
\hat{\kappa}_4(X_v) &= \frac{1}{n(n-1)(n-2)(n-3)} \Big((n^3 + n^2) S_4 - 4(n^2 + n) S_3 S_1 \\
&\qquad - 3(n^2 - n) S_2^2 + 12 n S_2 S_1^2 - 6 S_1^4 \Big),
\end{aligned} \tag{6.2}$$

or by fitting a parametric distribution to the marginal distribution of X_v and use the parametric form of the cumulants in this estimated distribution. In the above equations, n is the number of observations and $S_i = \sum_{v \in \mathcal{V}} x_v^i$.

7 Data example revisited

In this section, we investigate whether a normal inverse Gaussian random field provides a better fit to the data presented in Section 4. The covariance model is still the Matérn covariance model. Let $\theta = (\alpha, \beta, \mu, \delta)$ be the parameters of the normal inverse Gaussian Lévy basis and let $\kappa_n(\theta)$ be the parametric form of the cumulants of a random variable with this distribution, see Table 2, right column. We then estimated θ by solving the non-linear equations

$$\hat{\kappa}_n = \kappa_n(\theta) \int_{\mathbb{R}^3} \hat{k}(v,u)^n \, \mathrm{d}u, \quad n = 1, 2, 3, 4,$$

with respect to θ. The integral $\int_{\mathbb{R}^3} \hat{k}(v,u)^n \, \mathrm{d}u$ is known in analytic form for $n = 2$, cf. (3.3), while for $n = 3$ and 4, numerical integration was performed in Mathematica.

We used two methods of determining estimates $\hat{\kappa}_n$ of the cumulants of X_v, a non-parametric method, using (6.2), and a semi-parametric method where a normal inverse Gaussian distribution was fitted by the EM algorithm directly to the data $\{x_v : v \in \mathcal{V}\}$. If we let $\hat{\theta}_0$ be the estimated parameter of the normal inverse Gaussian distribution fitted by the EM algorithm to the distribution of the x_vs, we then refitted a Matérn covariance model to the empirical variogram, now normalized with $\hat{\kappa}_2(\hat{\theta}_0)$. A figure showing the empirical variogram normalized with $\hat{\kappa}_2(\hat{\theta}_0)$ and its Matérn fit together with the variogram normalized with the empirical variance and its corresponding Matérn fit, are shown in Figure 4. The two methods produce fits of comparable quality to the empirical variograms.

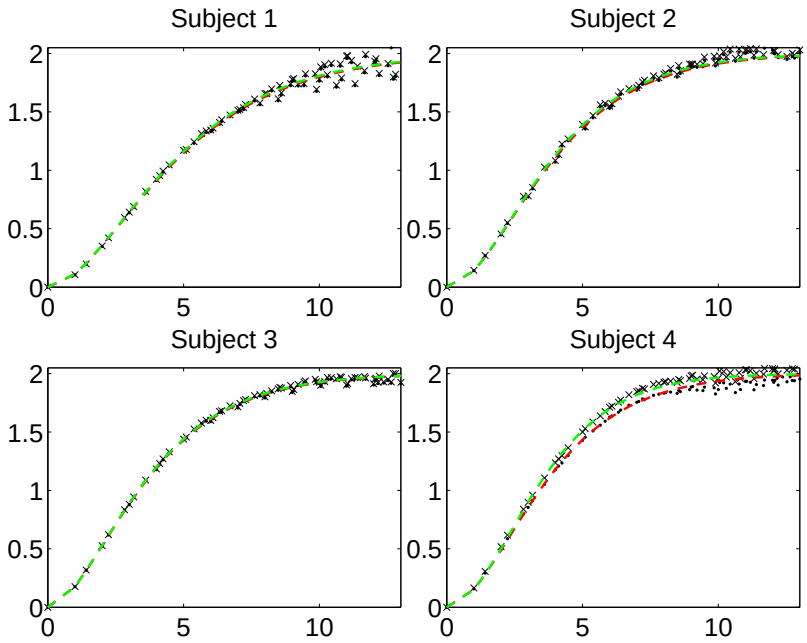

Figure 4: The estimated variogram normalized with the model based variance estimate ($\times$) together with a fitted Matérn variogram model (green) are shown for each of the four subjects. The estimated variogram normalized with the empirical variance ($\bullet$) and its associated fitted Matérn variogram model (red) are also shown.

Table 3: The estimates of the parameters of a normal inverse Gaussian random field model with a Matérn covariance structure, using non-parametric and semi-parametric estimation.

Subject	Method	$\hat{\alpha}$	$\hat{\beta}$	$\hat{\mu}$	$\hat{\delta}$	$\hat{\nu}$	$\hat{\lambda}$
1	Non-parametric	0.0111	0.0064	−2.0127	2.8583	1.5700	0.3971
	Semi-parametric	0.0113	0.0059	−1.9007	3.1041	1.6179	0.4094
2	Non-parametric	0.0260	0.0145	−1.2282	1.8321	1.9345	0.5477
	Semi-parametric	0.0605	0.0428	−2.4025	2.4004	2.0715	0.5795
3	Non-parametric	0.0203	0.0096	−1.6696	3.0894	1.5660	0.5162
	Semi-parametric	0.0469	0.0326	−3.6205	3.7466	1.6065	0.5281
4	Non-parametric	0.0306	0.0240	−1.6647	1.3088	2.0054	0.5938
	Semi-parametric	0.0314	0.0207	−1.4767	1.6747	2.8686	0.7759

In Table 3, the estimated parameters θ of the normal inverse Gaussian Lévy basis and ν and λ of the kernel function are shown for each of the four subjects analyzed in Section 4 and the two methods of estimation (non-parametric and semi-parametric).

In Figure 5, the observed distribution of X_v (shown as $\times$) is shown for each of the four subjects with the fitted distribution described by the model equation (5.2) and the estimated parameters $\hat{\theta}$, $\hat{\nu}$ and $\hat{\lambda}$. Both the non-parametric (blue line) and the semi-parametric (green line) fit are shown as well as the fit obtained, using a Gaussian random field (red line). Since the density of X_v under the model (5.2) with a Matérn kernel and a normal inverse Gaussian Lévy basis is not known analytically, the blue and green curves in Figure 5 have been determined by simulation. Note that a log-scale on the $y-$axis is used in Figure 5. The normal inverse Gaussian random fields model provides a more satisfactory fit.

Figure 6 shows simulations of the normal inverse Gaussian random field, fitted by the semi-parametric method, together with simulations of the Gaussian random field, fitted as described in Section 4, and the observed random field in slice 1, 2 and 3, respectively, for subject 4. It is seen that the NIG based simulations capture more satisfactory the feature of the data that occasionally very high values are observed at some voxels.

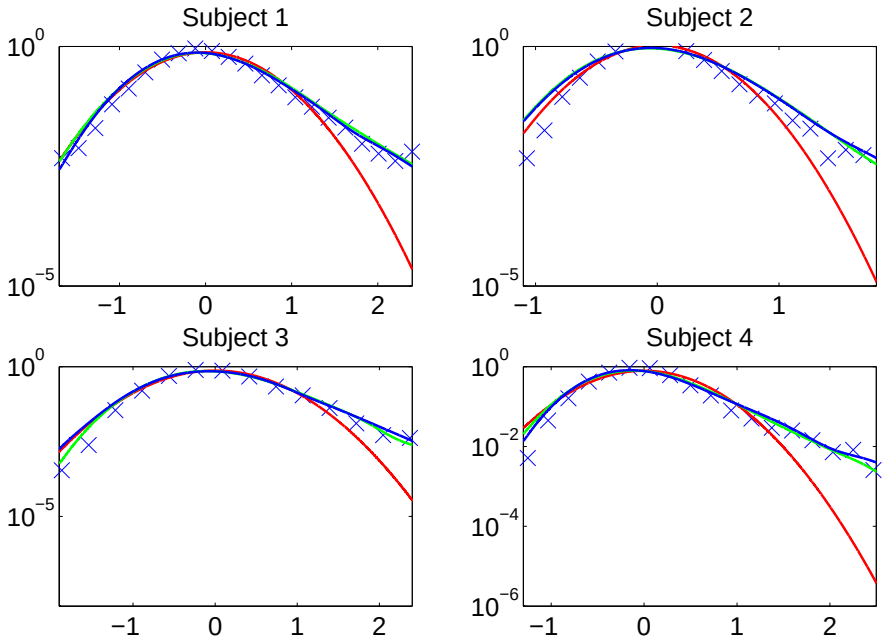

Figure 5: Log-histograms for the data (×) in the selected region for four healthy subjects together with the fitted Gaussian densities and the densities based on a NIG (normal inverse Gaussian) random field model. The Gaussian density is shown as the red curve, the NIG based density estimated using the method of moments is shown as the blue curve and the NIG based density estimated using the EM algorithm is shown as the green curve.

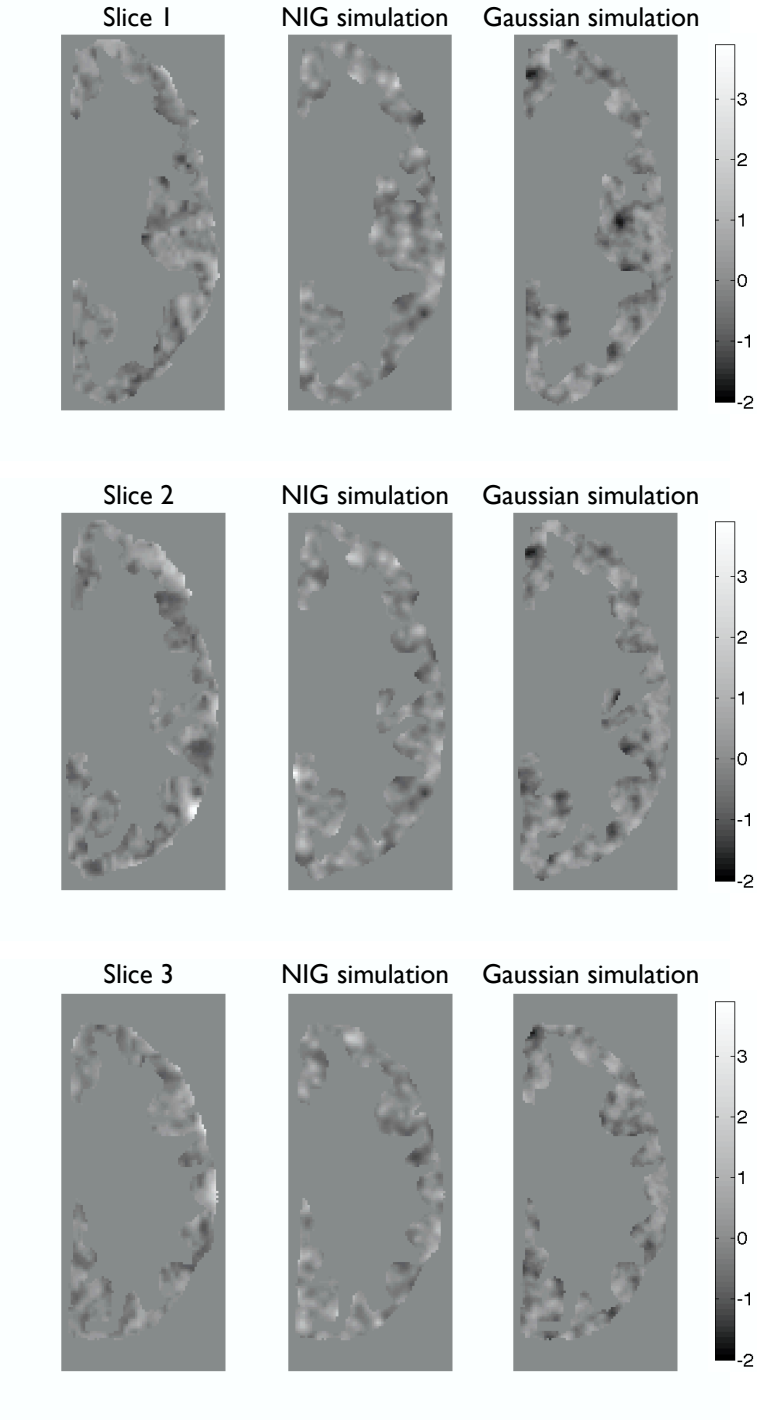

Figure 6: Observed MTT measurements (left) together with simulations under the fitted NIG model (middle) and the fitted Gaussian model (right) for subject 4.

8 Consequences for brain imaging

8.1 Voxel-wise comparisons

As indicated in the Introduction of our paper, a widely used procedure in brain imaging for testing the hypothesis of no difference between two groups of subjects is the following. Assume that we want to compare two groups of N subjects. Let X_{ijv} be the measurement recorded at voxel $v \in \mathcal{V}$ of the jth subject in group i, $i = 1, 2$, $j = 1, \ldots, N$. At each voxel the $t-$test statistic of no difference between the groups is determined

$$T_v = \frac{\bar{X}_{2\cdot v} - \bar{X}_{1\cdot v}}{\sqrt{2S_v^2/N}},$$

where $\bar{X}_{i\cdot v}$ is the average in group $i = 1, 2$ and

$$S_v^2 = \frac{1}{2N-2} \sum_{i,j} (X_{ijv} - \bar{X}_{i\cdot v})^2$$

is the estimate of the variance at voxel v, respectively.

If the alternative hypothesis is that group 2 subjects show increased level compared to group 1 subjects at some voxels, a common practice is to consider the distribution of the observed maximal test statistic $T_{\max} = \max\{T_v : v \in \mathcal{V}\}$ under the null hypothesis of no difference between the groups and to reject the null hypothesis at voxel v if $T_v > t_{\max 95}(\text{Gauss})$. Here, $t_{\max 95}(\text{Gauss})$ is the 95 percentile in the distribution of $T_{\max}$ calculated under the null hypothesis and under the assumption that the observed random fields can be modelled as Gaussian random fields. For Gaussian random fields, the 95 percentile can be estimated using the Euler characteristic of excursion sets of thresholded t fields but below we use a bootstrap technique. (Note that by using $T_{\max}$, the so-called family wise error (FWE) is controlled as opposed to the false discovery rate (FDR), see Chumbley and Friston (2009); Chumbley et al. (2010b); Nichols and Hayasaka (2003) and references therein.)

In order to evaluate the robustness of this procedure against departures from Gaussianity, we have simulated random fields of size 100×100 under the fitted Gaussian random field model *and* under the fitted normal inverse Gaussian random field model for subject 4, see bottom row in Table 1 and Table 3. We simulated a total of 100 images from each model and estimated the null distribution of the test statistic $T_{\max}$ for the various group sizes N, using a bootstrap technique.

In Figure 7, the difference $t_{\max 95}(\text{Gauss}) - t_{\max 95}(\text{NIG})$ is plotted as a function of the number N of subjects in each group. Here, $t_{\max 95}(\text{NIG})$ is the 95 percentile in the distribution of $T_{\max}$ calculated under the null hypothesis and under the assumption that the observed random fields can be modelled by normal inverse Gaussian random fields. The difference between the percentiles is positive for all N and largest for small N. So for small group sizes N, we may overlook an increased signal in group 2 compared to group 1 if the fields are normal inverse Gaussian but wrongly assumed to be Gaussian.

For illustrating how much impact the difference in the 95 percentiles of the distribution of $T_{\max}$ may have, we added in group 2 a signal of strength s in a

subregion of size 20×20 voxels and estimated the average proportion of the subregion that was correctly declared as significant, using the NIG threshold and the Gaussian threshold, respectively.

The average proportion was calculated using a bootstrapping technique. The results are shown in Figure 8. We see that in either case, no or few voxels are declared significant for small values of N and/or a low signal strength s. For larger signal strengths s and a large number N of subjects in each group, both methods declare the majority of the signal significant. For intermediate values of N and s the NIG threshold shows superior performance, see Figure 8 (right). For instance, for $s = 2$ and $N = 10$, the average proportion declared significant is 0.8727 and 0.5832, using the NIG and Gaussian threshold, respectively. In this case, a much larger part of the signal is detected if the NIG threshold is used.

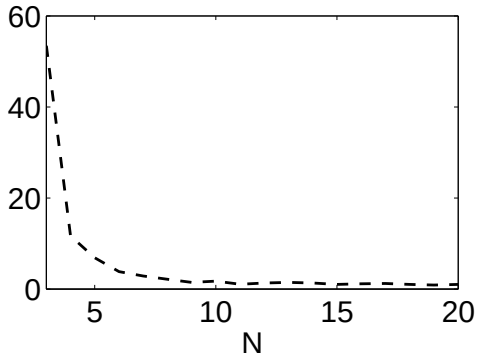

Figure 7: The difference $t_{\max 95}(\text{Gauss}) - t_{\max 95}(\text{NIG})$ as a function of the number N of subjects in each group.

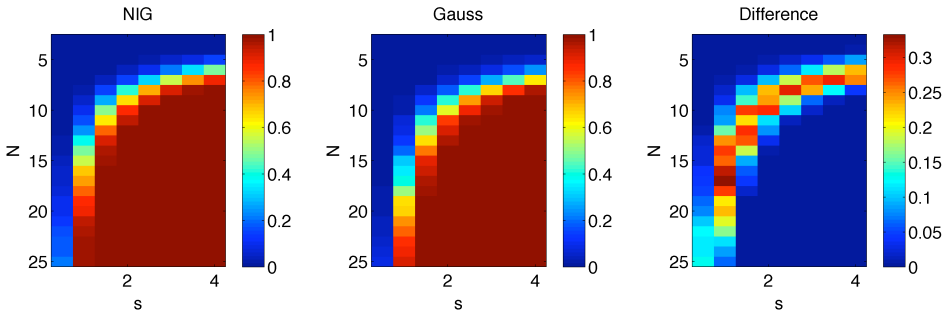

Figure 8: The average proportion of a subregion of size 20×20 voxels with signal strength s that is declared significant using the NIG threshold (left) and the Gaussian threshold (middle), shown as a function of s and the group size N. The difference in the proportion of the subregion declared significant using the two methods is also shown as a function of s and the group size N (right).

8.2 Region-wise comparisons

Lévy based random fields may also strengthen another type of analysis often performed in neuroscience, so-called ROI (Region Of Interest) analysis (Chumbley et al.

2010a; Friston et al. 1994). Again, two groups of subjects are compared, this time with the aim of revealing whether the overall level of the signal in a specific region of the brain is increased in one group compared to the other. A proper modelling of the correlation structure in the field may be used to construct optimally weighted average signals with minimal variance in each group, thereby increasing the possibility for detecting small differences in the signal level in the two groups. This has already been advocated in Spence et al. (2007). See also Bowman (2007), where functional distances is used instead of Euclidean distances in the covariance structure. In addition, the Lévy based random fields offer the possibility to analyze changes that imply that the distribution of the signal is more skewed or has more heavy tails in one group compared to the other.

9 Discussion

In the present paper, we have mainly been focusing on developing Lévy based random fields as a practical statistical tool of analyzing images, especially brain images. Earlier, this type of model has also been used as prior in non-parametric function estimation, see Tu et al. (2007). We have advocated Lévy based random fields as a flexible class of models for random fields. A more specific class of skew-Gaussian random fields has been described in Alodat and Al-Rawwash (2009).

In the analysis of the magnetic resonance imaging data presented in Sections 4 and 7, we found that the observed random fields were markedly non-Gaussian and, using Gaussian random field theory, may lead to incorrect conclusions when comparing small groups of subjects. Similar type of conclusion has been reached in a number of fMRI studies (Nichols and Hayasaka 2003).

In the concrete data analysis, the normal inverse Gaussian random field model provided a satisfactory fit. We believe that it is interesting to study this type of random field further from a theoretical point of view. Especially, it should be investigated whether the properties of the excursion sets of such random fields can be derived by conditioning with its associated stochastic variance field.

Acknowledgements

The authors thank Torben Lund and Ole E. Barndorff-Nielsen for fruitful discussions. This research has been supported by MINDLab and Centre for Stochastic Geometry and Advanced Bioimaging, funded by the Villum Foundation.

References

Abramowitz, A. and Segun, I. (1968). *Handbook of Mathematical Functions*. Dover Publications, New York.

Adhya, S., Johnson, G., Herbert, J., Jaggi, H., Babb, J., Grossman, R., and Inglese, M. (2006). Pattern of Hemodynamic Impairment in Multiple Sclerosis: Dynamic Susceptibility Contrast Perfusion MR Imaging at 3.0 T. *Neuroimage*, 33:1029–1035.

Adler, R., Samorodnitsky, G., and Taylor, J. (2010a). Excursion sets of three classes of stable random fields. *Advances in Applied Probability*, 42:293–318.

Adler, R., Samorodnitsky, G., and Taylor, J. (2010b). High level excursion set geometry for non-gaussian infinitely divisible random fields. Submitted.

Alodat, M. and Al-Rawwash, M. (2009). Skew-gaussian random field. *Journal of Computational and Applied Mathematics*, 232:496–504.

Barndorff-Nielsen, O. (1998). Processes of normal inverse gaussian type. *Finance and Stochastics*, 2:41–68.

Barndorff-Nielsen, O. (2010). Lévy basis and extended subordination. Research report 12, Thiele Centre, Department of Mathematical Sciences, Aarhus University.

Barndorff-Nielsen, O. and Pedersen, J. (2010). Meta-times and extended subordination. Research report 15, Thiele Centre, Department of Mathematical Sciences, Aarhus University.

Barndorff-Nielsen, O. and Schmiegel, J. (2004). Lévy based tempo-spatial modeling; with applications to turbulence. *Uspekhi Mat. Nauk*, 159:63–90.

Bowman, F. (2007). Spatiotemporal models for region of interest analyses of functional neuroimaging data. *Journal of the American Statistical Association*, 102:442–453.

Cao, J. (1999). The size of the connected components of excursion sets of χ^2, t and f fields. *Advances in Applied Probability*, 31:579–595.

Chumbley, J., Flandin, G., Seghier, M., and Friston, K. (2010a). Multinomial inference on distributed responses in spm. *NeuroImage*, 53.

Chumbley, J. and Friston, K. (2009). False discovery rate revisited: Fdr and topological inference using gaussian random fields. *NeuroImage*, 44:62–70.

Chumbley, J., Worsley, K., Flandin, G., and Friston, K. (2010b). Topological fdr for neuroimaging. *NeuroImage*, 49:3057–3064.

Cressie, N. (1993). *Statistics for Spatial Data*. Wiley, New York.

Friston, K., Worsley, K., Frackowiak, R., Mazziotta, J., and Evans, A. (1994). Assessing the significance of focal activations using their spatial extent. *Human Brain Mapping*, 1:214–220.

Gaetan, C. and Guyon, X. (2010). *Spatial Statistics and Modeling*. Springer, New York.

Guttorp, P. and Gneiting, T. (2006). Studies of the history of probability and statistics xlix on the matérn correlation family. *Biometrika*, 93:989–995.

Helenius, J., Perkiö, J., Soinne, L., Ø stergaard, L., Carano, R., Salonen, O., Savolainen, S., Kaste, M., Aronen, H., and Tatlisumak, T. (2003). Cerebral hemodynamics in a healthy population measured by dynamic susceptibility constrast mr imaging. *Acta Radiologica*, 44:538–546.

Hellmund, G., Prokešová, M., and Jensen, E. (2008). Lévy-based Cox point processes. *Advances in Applied Probability*, 40:603–629.

Ibaraki, M., Ito, H., Shimosegawa, E., Toyoshima, H., Ishigame, K., Takahashi, K., Kanno, I., and Miura, S. (2007). Cerebral vascular mean transit time in heathy humans: a comparative study with pet and dynamic susceptibility contrast-enhanced mri. *Journal of Cerebral Blood Flow & Metabolism*, 27.

Ito, H., Kanno, I., Takahashi, K., Ibaraki, M., and Miura, S. (2003). Regional distribution of human cerebral vascular mean transit time measured by positron emission tomography. *NeuroImage*, 19:1163–1169.

Jónsdóttir, K., Schmiegel, J., and Jensen, E. (2008). Lévy-based growth models. *Bernoulli*, 14:62–90.

Kendall, M. and Stuart, A. (1976). *The Advanced Theory of Statistics. Vol. 1. Distribution Theory*. Griffin, London, fourth edition edition.

Lord, R. (1954). The use of the hankel transform in statistics. i. general theory and examples. *Biometrika*, 41:44–55.

Luckhaus, C., Flüss, M., Wittsack, H.-J., Grass-Kapanke, B., Jänner, M., Khalili-Amiri, R., Friedrich, W., Supprian, T., Gaebel, W., Mödder, U., and Cohnen, M. (2008). Detection of changed regional cerebral blood flow in mild cognitive impairment and early alzheimer's dementia by perfusion-weighted magnetic resonance imaging. *NeuroImage*, 40:495–503.

Lythgoe, D., Ø stergaard, L., Williams, S., Cluckie, A., Buxton-Thomas, M., Simmons, A., and Markus, H. (2000). Quantitative perfusion imaging in carotid artery stenosis using dynamic susceptibility contrast-enhanced magnetic resonance imaging. *Magnetic Resonance Imaging*, 18:1–11.

Nichols, T. and Hayasaka, S. (2003). Controlling the familywise error rate in functional neuroimaging: a comparative review. *Statistical Methods in Medicine*, 12:419–446.

Nichols, T. and Holmes, A. (2001). Nonparametric permutation tests for functional neuroimaging: a primer with examples. *Human Brain Mapping*, 15:1–25.

Østergaard, L., Weisskoff, R., Chesler, D., Gyldensted, C., and Rosen, B. (1996). High resolution measurement of cerebral blood flow using intravascular tracer bolus passages. part i. mathematical approach and statistical analysis. *Magnetic Resonance in Medicine*, 36:715–725.

Salmond, C., Ashburner, J., Vargha-Khadem, F., Connelly, A., Gadian, D., and Friston, K. (2002). Distributional assumptions in voxel-based morphometry. *NeuroImage*, 17:1027–1030.

Spence, J., Carmack, P., Gunst, R., Schucany, W., Woodward, W., and Haley, R. (2007). Accounting for spatial dependence in the analysis of spect brain imaging data. *Journal of the American Statistical Association*, 102:464–473.

Tu, C., Clyde, M., and Wolpert, R. (2007). Lévy adaptive regression kernels. Technical report, Duke University, Department of Statistical Sciences.

Viviani, R., Beschoner, P., Ehrhard, K., Schmitz, B., and Thöne, J. (2007). Non-normality and transformations of random fields, with an application to voxel-based morphometry. *NeuroImage*, 35:121–130.

Wolpert, R. (2001). Lévy moving averages and spatial statistics. Lecture available at `http://citetseer.ist.psu.edu/ wolpert01leacutevy.html`.

Worsley, K. (1994). Local maxima and the expected euler characteristic of excursion sets of χ^2, f and t fields. *Advances in Applied Probability*, 26:13–42.

Worsley, K., Evans, A., Marrett, S., and Neelin, P. (1992). A three dimensional statistical analysis for cbf activations studies in human brain. *J. Cerebral Blood Flow and Metabolism*, 12:900–918.

Worsley, K., Marrett, S., Neelin, P., Vandal, A., Friston, K., and Evans, A. (1996). A unified statistical approach for determining significant signals in images of cerebral activation. *Human Brain Mapping*, 4:58–73.

Wu, O., Østergaard, L., Schaefer, P., Rosen, B., Weisskoff, R., and Sorensen, A. (2003). Tracer arrival timing insensitive technique for estimating flow in mr perfusion-weighted imaging using singular value decomposition with a block-circulant deconvolution matrix. *Magnetic Resonance in Medicine*, 50:856–864.

Appendix: Derivations for the Matérn family

Under the Lévy based random field model we have that the covariance function is given by

$$C(h) = \mathrm{Var}(Z') \int_{\mathbb{R}^d} k(u)k(h+u)\,\mathrm{d}u.$$

The spectral density of the random field is given by

$$f(\omega) = \frac{1}{(2\pi)^d} \int_{\mathbb{R}^d} C(h)e^{-i\omega\cdot h}\,\mathrm{d}h = \frac{1}{(2\pi)^d}\ \mathrm{Var}(Z') \Big(\int_{\mathbb{R}^d} k(h)e^{-i\omega\cdot h}\,\mathrm{d}h\Big)^2.$$

It follows that

$$k(u) = \frac{1}{\sqrt{\mathrm{Var}(Z')(2\pi)^d}} \int_{\mathbb{R}^d} \sqrt{f(h)}e^{iu\cdot h}\,\mathrm{d}h. \tag{9.1}$$

One parametrization of the Matern correlation family is given by a correlation of the type

$$\rho(h) = \frac{2^{1-\nu}}{\Gamma(\nu)}(\lambda\|h\|)^\nu K_\nu(\lambda\|h\|), \tag{9.2}$$

for $\nu, \lambda > 0$, cf. Guttorp and Gneiting (2006), which corresponds to the spectral density

$$f(\omega) \propto \frac{1}{(\lambda^2 + \|\omega\|^2)^{d/2+\nu}}. \tag{9.3}$$

Now using equation (9.1) for the spectral density in (9.3) we find that

$$k(u) \propto \int_{\mathbb{R}^d} p(\|h\|) e^{iu\cdot h}\,\mathrm{d}h, \tag{9.4}$$

where

$$p(r) = \frac{1}{(\lambda^2 + r^2)^{d/4+\nu/2}}.$$

In Lord (1954), it is shown that an integral of this form can be expressed as

$$\int_{\mathbb{R}^d} p(\|h\|) e^{iu\cdot h}\,\mathrm{d}h = (2\pi)^{d/2}\|u\|^{1-d/2}\int_0^\infty r^{d/2} J_{d/2-1}(\|u\|r)p(r)\,\mathrm{d}r, \tag{9.5}$$

where $J_{d/2-1}$ is a Bessel function of the first kind. Further reduction can be obtained by using that, cf. Abramowitz and Segun (1968, (11.4.44)),

$$\int_0^\infty \frac{t^{\beta+1}J_\beta(at)}{(t^2+z^2)^{\mu+1}}dt = \frac{a^\mu z^{\beta-\mu}}{2^\mu\Gamma(\mu+1)}K_{\beta-\mu}(az), \tag{9.6}$$

which holds for $a > 0$, $\beta > -1$ and $\beta < 2\mu + 3/2$. These inequalities are satisfied in our case and we find by combining (9.4), (9.5) and (9.6) that

$$\begin{aligned} k(u) &\propto \|u\|^{1-d/2}\int_0^\infty r^{d/2}J_{d/2-1}(\|u\|r)\frac{1}{(\lambda^2+r^2)^{d/4+\nu/2}}\,\mathrm{d}r \\ &\propto \|u\|^{\nu/2-d/4}K_{d/4-\nu/2}(\lambda\|u\|) = \|u\|^{\nu/2-d/4}K_{\nu/2-d/4}(\lambda\|u\|). \end{aligned}$$

The constant of proportionality can be determined by using that

$$\int_{\mathbb{R}^d} k(u)\,\mathrm{d}u = 1.$$

Let $\omega_d = 2\pi^{d/2}/\Gamma(d/2)$ denote the surface area of the unit sphere in $\mathbb{R}^d$. Then

$$\begin{aligned} &\int_{\mathbb{R}^d} \|u\|^{\nu/2-d/4}K_{\nu/2-d/4}(\lambda\|u\|)\,\mathrm{d}u \\ &\quad= \omega_d\int_0^\infty r^{\nu/2-1+3d/4}K_{\nu/2-d/4}(\lambda r)\,\mathrm{d}r \\ &\quad= \Gamma\Big(\frac{\nu+d/2}{2}\Big)\frac{\pi^{d/2}2^{\nu/2-1+3d/4}}{\lambda^{\nu/2+3d/4}}, \end{aligned}$$

where we at the last equality sign have used the identity

$$\int_0^\infty t^\mu K_\beta(t)dt = 2^{\mu-1}\Gamma\Big(\frac{\mu+\beta+1}{2}\Big)\Gamma\Big(\frac{\mu-\beta+1}{2}\Big), \tag{9.7}$$

cf. Abramowitz and Segun (1968, (11.4.22)). The identity (9.7) holds for $\mu\pm\beta > -1$. This condition is satisfied for our choice of parameters if $d \geq 2$. Consequently the kernel function is given by

$$k(u) = \frac{\lambda^d}{\pi^{d/2}2^{\nu/2-1+3d/4}\Gamma\big(\frac{\nu+d/2}{2}\big)}\|\lambda u\|^{\nu/2-d/4}K_{\nu/2-d/4}(\lambda\|u\|).$$

In order to use the cumulant relations for the Lévy based random fields, we need to determine $\int_{\mathbb{R}^d} k(u)^n \,\mathrm{d}u$. For $n = 2$, we use that

$$\int_0^\infty t^{\alpha-1} K_\beta(t)^2 \,\mathrm{d}t = \frac{\sqrt{\pi}}{4\Gamma(\frac{\alpha+1}{2})} \Gamma\Big(\frac{\alpha}{2}\Big)\Gamma\Big(\frac{\alpha}{2}-\beta\Big)\Gamma\Big(\frac{\alpha}{2}+\beta\Big),$$

for $\alpha > 2|\beta|$, and find

$$\begin{aligned}\int_{\mathbb{R}^d} k(u)^2 \,\mathrm{d}u &= \frac{\lambda^d}{\pi^{d/2} 2^{\nu-3+3d/2} \Gamma(\frac{\nu+d/2}{2})^2 \Gamma(d/2)} \int_0^\infty t^{\nu+d/2-1} K_{\nu/2-d/4}(t)^2 \,\mathrm{d}t \\ &= \frac{\lambda^d \Gamma(\nu)}{\pi^{d/2} 2^d \Gamma(\nu + d/2)},\end{aligned}$$

where we at the last equality sign also have used that

$$\Gamma(x)\Gamma(x+1/2) = 2^{1-2x}\sqrt{\pi}\Gamma(2x).$$

Note that the explicit form of the covariance function follows easily

$$\begin{aligned}C(h) = C(0)\rho(h) &= \mathrm{Var}(Z') \int_{\mathbb{R}^d} k(u)^2 \,\mathrm{d}u \cdot \rho(h) \\ &= \frac{\mathrm{Var}(Z')\lambda^d}{\pi^{d/2} 2^{d+\nu-1} \Gamma(\nu + d/2)} (\lambda\|h\|)^\nu K_\nu(\lambda\|h\|).\end{aligned}$$

For $n > 2$, it is only possible in special cases to derive an explicit form of $\int_{\mathbb{R}^d} k(u)^n \,\mathrm{d}u$. In any case, the integral can be expressed as an integral over $\mathbb{R}_+$. If we let

$$\gamma_{d,\nu} = \frac{\lambda^d}{\pi^{d/2} 2^{\nu/2-1+3d/4} \Gamma\big(\frac{\nu+d/2}{2}\big)}$$

we get

$$\int_{\mathbb{R}^d} k(u)^n \,\mathrm{d}u = \gamma_{d,\nu}^n \,\omega_d \,\frac{1}{\lambda^d} \int_0^\infty r^{n\nu/2+(1-n/4)d-1} K_{\nu/2-d/4}(r)^n \,\mathrm{d}r.$$

For $n = 3$, this integral is finite for $d = 2$ and $\nu > 1/3$ and for $d = 3$ and $\nu > 1/2$. For $n = 4$, the integral is finite for $d = 2$ and $\nu > 1/2$ and for $d = 3$ and $\nu > 3/4$.

The modified Bessel function of the second kind K_ν has nice analytic expressions for specific ν. Thus, cf. Abramowitz and Segun (1968, (10.2.17)),

$$\begin{aligned}K_{1/2}(x) &= \sqrt{\frac{\pi}{2x}} e^{-x}, \\ K_{3/2}(x) &= \sqrt{\frac{\pi}{2x}} e^{-x} \left(1 + \frac{1}{x}\right), \\ K_{5/2}(x) &= \sqrt{\frac{\pi}{2x}} e^{-x} \left(\frac{3}{x^2} + \frac{3}{x} + 1\right).\end{aligned}$$

For $\nu = 1/2$, the exponential covariance function is obtained while for $\nu = 5/2$ we get the 3rd order autoregressive covariance function.